Materials and Design 180 (2019) 107958

Contents lists available at ScienceDirect

Materials and Design

journal homepage: www.elsevier.com/locate/matdes

On the interplay between intermetallic controlled growth and hot tearing susceptibility in Al-to-steel welding with additional interlayers

N. Jimenez-Mena, A. Simar *, P.J. Jacques

Université catholique de Louvain, Institute of Mechanics, Materials and Civil Engineering, IMAP, 1348 Louvain-la-Neuve, Belgium

HIGHLIGHTS

- The thickness of the intemetallic layer in Al-to-steel welding is greatly reduced with the use of Co and Ni interlayers
- Dissolution of the interlayer in liquid aluminium changes the behaviour of the latter and bring the formation of hot tears
- A model for interlayer dissolution in liquid aluminium combined to a hot tearing criterion predicts the experimental results

GRAPHICAL ABSTRACT

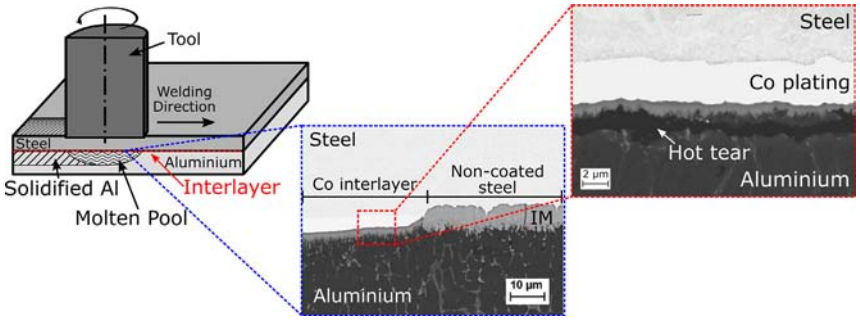

ARTICLE INFO

Article history:
Received 26 April 2019
Received in revised form 11 June 2019
Accepted 19 June 2019
Available online 20 June 2019

Keywords:
Dissimilar welding
Friction melt bonding
Aluminium
Steel
Hot tearing
Dissolution

ABSTRACT

The brittle behaviour of Fe/Al intermetallic compounds formed during dissimilar Al-to-steel welding is a major drawback for the mechanical integrity of the joint, particularly for thick intermetallic layers. In order to improve the toughness of the weld, the control of the thickness and the nature of the intermetallic layer have been investigated owing to the addition of an electroplated nickel or cobalt interlayer prior to welding by the novel Friction Melt Bonding (FMB) process. The FMB joining of DP600 steel and AA1050 is achieved by the wetting and reaction of liquid aluminium to the solid steel surface and subsequent solidification. Nevertheless, hot tears, also appear owing to the dissolution of the interlayer in the liquid aluminium. The dissolution and diffusion of the interlayer has been analysed and modelled using the second Fick's diffusion law when imposing a kinetic dissolution behaviour at the interface. The risk of hot tearing was assessed using the Scheil-Gulliver model to calculate the solidification path and a composition-based hot tearing criterion. As a result of the dissolution of the interlayer, the composition of the molten pool evolves, which leads to changes in the nature, morphology and thickness of the reaction interlayer.

1. Introduction

One of the strategies to decrease the fuel consumption by the transport sector would be to reduce the weight of the vehicle structures while keeping strength, formability and crashworthiness to ensure the safety of the passengers. This goal can be achieved with multi-material structures where the best properties of different materials, like aluminium and steel, are efficiently combined [1,2]. Hence, dissimilar welding methods have to be developed to give answers to these requirements.

The complexity of aluminium-to-steel welding lays in their different metallurgical and mechanical profiles. The aluminium-iron binary phase diagram [3] reveal three main challenges: (i) the large difference in melting temperatures of aluminium and iron, (ii) the low solubility

* Corresponding author.
E-mail address: aude.simar@uclouvain.be (A. Simar).

https://doi.org/10.1016/j.matdes.2019.107958

Nomenclature

Symbol	Description Units
C_{int}, C_{liquid}	Concentration of the dissolved species at the interface and in the liquid Al, respectively at.%
C^s_{liq}	Solubility of the dissolved species in liquid Al at equilibrium at.%
$D(\theta)$	Diffusion coefficient of the solute in liquid Al $m^2\ s^{-1}$
D_o	Pre-exponential constant for diffusion $m^2\ s^{-1}$
E_D	Energy activation for diffusion $J\ mol^{-1}$
$f_s(\theta)$	Solid fraction –
k	Dissolution rate s^{-1}
P	Power generated by the tool W
R	Gas constant $J\ mol^{-1}\ K^{-1}$
S	Surface in contact with the liquid m^2
t	Time s
T_z	Torque on the tool N m
V	Volume of the molten pool m^3
x	Distance from the interface m
η	Efficiency of the heat generation on the tool –
θ	Temperature °C
ω	Rotational speed of the tool $rad\ s^{-1}$

between aluminium and iron, and (iii) the formation of brittle Fe/Al intermetallic compounds (IM) at the reacting interface [4–6]. According to Tanaka et al. [4], the thickness of the IM layer determines the interface toughness of Al-to-steel welds. They measured the tensile bonding strength in the case of friction stir welds and concluded that the toughness is inversely proportional to the IM thickness for thicknesses below 1 μm, while larger thicknesses deteriorate the weld toughness.

In practice, dissimilar Al-to-steel welding processes can be split into two categories whether or not the aluminium melts. In solid-state processes such as Friction Stir Welding (FSW) [4,6] or friction welding [7], solid Al reacts with solid steel to form the Al/Fe IM layer due to the exposure of oxide-free fresh surfaces and the rise of temperature generated by severe deformation of the base materials. By keeping the temperature below the solidus temperature of the aluminium, the IM growth is easily controlled and thicknesses below 1 μm can be achieved [4]. If the aluminium melts and the steel remains solid owing to the large difference in melting temperatures, the plates are welded by reactive wetting. This is the case for arc welding [8], laser welding in conduction mode [9,10] and resistance spot welding [11]. The temperatures reached in the case of reactive wetting processes are higher than in solid-state processes, bringing faster IM growth rates and thus leading to thicker IM layers. However, the high reactivity of liquid aluminium and solid steel allows for faster welding speeds.

Two main strategies are used to control the thickness of the intermetallic layer. The first one consists in controlling the heat input [12–14]. The second one consists in using an interlayer as a diffusional barrier to either avoid or control the formation of the IM layer. In a previous work, Jimenez-Mena et al. [14] used a Co interlayer in Friction Melt Bonding of AA1050 and Dual-Phase steel to increase the toughness of the weld. The interlayer promoted an intermetallic layer composed of Co-Al intermetallics with a thickness of the order of 1.5 μm. Reddy et al. [7] used copper, nickel and silver interlayers in the case of Al-to steel friction welding to change the nature of the IM. They observed that the interlayer improves the weld toughness. Kannan et al. [15] showed an improvement in the mechanical strength of friction welded Al-to-steel samples using a silver interlayer. Chen et al. [16] studied single-beam keyhole laser welding of aluminium to steel with a 0.1 mm Cu-foil interlayer. They reported a 30% increase of the strength in lap-shear loading when compared to welds without interlayer. In another work, Chen et al. [17] also reported a 7% increase of the strength of a keyhole laser weld performed with a 0.1 mm Ni interlayer. The choice of an interlayer to achieve low IM thicknesses should take into account two phenomena: (i) the growth kinetics of the IM compounds and (ii) the potential dissolution of the IM layer in the molten aluminium [18,19].

In the present study, Friction Melt Bonding (FMB) process has been used to study the influence of an interlayer in the interaction between solid steel and liquid aluminium. FMB is a novel process to weld in lap-joint configuration dissimilar materials showing large differences in melting temperature as in the case of aluminium and steel [5,20]. A schematic view of the process is shown in Fig. 1. In this process, a steel plate is placed over an aluminium plate. The steel plate is heated up by the friction of a rotating cylindrical tool pressed against its top surface. If the bottom surface of the steel reaches a temperature over the melting temperature of the aluminium, the latter locally melts and reacts with the steel to form a joint potentially made of an Al/Fe IM layer at the interface. The tool is then displaced on the surface of the steel to form a continuous weld beam. No shielding gas is required since the aluminium molten pool remains confined between the steel and the solid aluminium.

Furthermore, Van der Rest et al. [5], Crucifix et al. [12] and Jimenez-Mena et al. [21] reported the presence of hot tears in FMB welds. Hot tears are intergranular cracks nucleating and propagating at grain boundaries in the semi-solid state [22,23]. The formation of hot tears depends on the composition of the alloy and on the thermomechanical cycles during solidification. Van der Rest et al. [5] observed hot tears formed in the case of aluminium alloy AA2024 while no hot tears were observed in commercially pure AA1050. Crucifix et al. [12] observed that the amount of hot tears increased with increasing welding speed. Jimenez et al. [21] used the criterion developed by Rappaz et al. [24] to predict the formation of hot tears in the case of FMB of AA6061 to Dual-Phase steel as a function of the welding parameters.

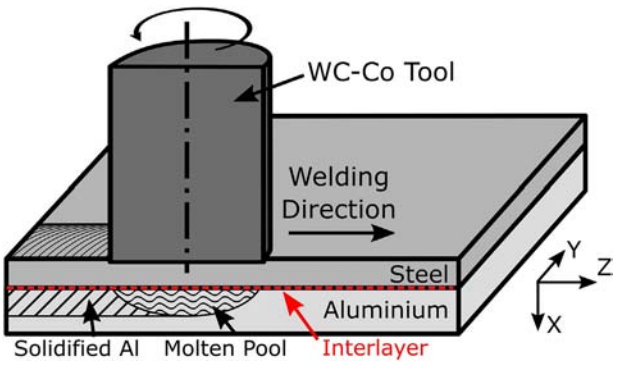

Fig. 1. Schematic representation of the FMB process. The electroplated interlayer is placed at the interface between the steel and aluminium plates.

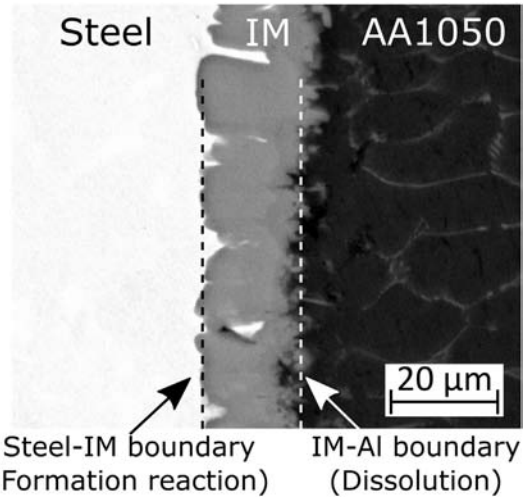

Fig. 2. SEM observation of the cross section of the interface. The formation of the interface occurs at the IM-steel interface. The dissolution of the IM in the liquid aluminium occurs at the IM-aluminium interface.

The hot tears observed in FMB joints with Co interlayer performed by Jimenez et al. [14] are due to the dissolution of the interlayer in the aluminium alloy. This dissolved interlayer changes the solidification behaviour of the aluminium alloy increasing the hot tearing susceptibility and reducing the toughness of the joint. Thus, in order to obtain sound FMB welds, not only a thin IM layer is required but also hot tears should be avoided. To predict and increase the soundness of FMB welds an integrated approach is suggested. It combines: (i) the control of thermomechanical cycles to form thin IM layers [12] and avoid solidification defects [21], and (ii) the use of an interlayer to limit the growth of the IM layer [14]. Currently, this approach lacks from a model allowing to predict the influence of the interlayer in the hot tearing susceptibility of the aluminium alloy.

Hence, in this work, a tool is developed to assess the influence of the choice of the interlayer in the hot tear formation when welding DP600 steel to AA1050. A thermal finite elements (FE) model and the second Fick's law are used to predict the dissolution behaviour of the interlayer in the aluminium molten pool. The risk of hot tear formation owing to the dissolution of this interlayer is evaluated using Kou's criterion [23]. This approach is experimentally validated for Co and Ni interlayers. Finally, the criteria to successfully choose an interlayer for the FMB process are discussed.

2. Dissolution of the IM phase in liquid metal

The final thickness of the IM layer after welding is the result of two competitive phenomena: (i) the thickening of the IM layer owing to the reaction of a metal M with liquid aluminium to form an IM layer in contact with this liquid aluminium,

$$M_{(s)} + Al_{(l)} \rightarrow M_xAl_y + Al_{(l)} \quad (1)$$

(ii) the thinning of the IM layer owing to its dissolution in the liquid aluminium resulting in a liquid phase of dissolved metal and aluminium [19]

$$M_xAl_y + Al_{(l)} \rightarrow M_{(l)} + Al_{(l)} \quad (2)$$

The mobility of Al atoms compared to Fe in the Fe_2Al_5 lattice is much larger due to the mobility of vacancies along the c-axis through which the Al atoms diffuse [25,26]. Thus, the Al atoms diffuse through the IM layer to encounter the Fe atoms and react to form the IM layer. It has been observed that the c-axis of the Fe_2Al_5 lattice in FMB of Al6061 to DP980 is perpendicular to the interface between the base materials [27]. Therefore, the reaction of formation of the IM compounds occurs at the steel-IM boundary shown in Fig. 2 while the dissolution phenomenon takes place at the IM-aluminium boundary. Since each competitive phenomenon occurs at a different boundary, the IM layer formation and dissolution phenomena can be uncoupled. The present work focuses exclusively on the kinetics of IM dissolution at the IM-aluminium boundary during welding since it mostly affects the hot tear susceptibility.

According to Verhaeghe et al. [28], the dissolution of a solid in contact with a liquid involves two different mechanisms: (i) the dissolution reaction at the interface and (ii) the diffusion of the dissolved species within the liquid.

Due to the transient nature of the problem in welding, the IM-liquid interface is not at equilibrium. The flux of the dissolving species (i.e. Fe, Ni or Co) from the interface to the liquid aluminium is described by the Nernst-Shchukarev equation [28]:

$$\frac{dC_{int}}{dt} = k^{*S}/_{V}\left(C^{s}_{liq}(\theta) - C_{int}\right) \quad (3)$$

where
C_{int} is the concentration of the dissolving species at the interface, C^{s}_{liq} is the saturation concentration of the dissolving species at equilibrium, θ is the temperature, k^* is the dissolution rate, t is the time and S is the surface of solid in contact with a liquid metal of volume V. The Nernst-Shchukarev equation describes the increasing concentration of dissolved species with time in a liquid of volume V up to reaching the saturation concentration, C^{s}_{liq}. This concentration corresponds to the liquidus boundary of the phase diagram of the studied system and, therefore, is a function of temperature.

The diffusion of the dissolved species in the molten metal is modelled as a one dimensional problem using the Fick's second law:

$$\frac{dC_{liquid}}{dt} = D(\theta)\frac{d^2C_{liquid}}{dx^2} \quad (4)$$

where C_{liquid} is the concentration of the dissolved species in the liquid, $D(\theta)$ is the diffusion coefficient and x is the distance to the interface. $D(\theta)$ follows an Arrhenius behaviour [29,30]:

$$D(\theta) = D_0 e^{\left(-E_D/R\theta\right)} \quad (5)$$

where D_0 is the pre-exponential factor, E_D is the activation energy for diffusion and R is the gas constant. For the sake of simplicity, the

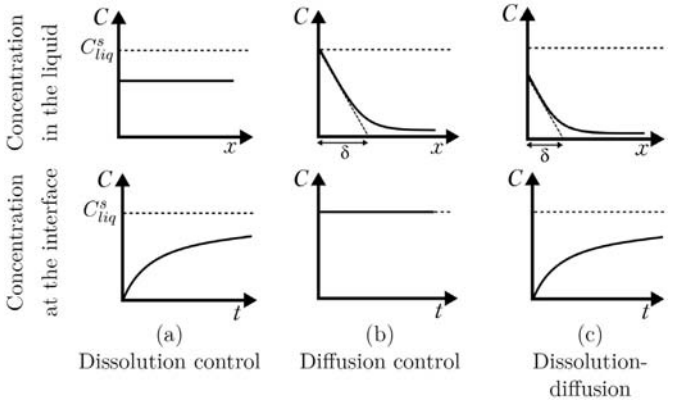

Fig. 3. Concentration profiles resulting from dissolution when (a) dissolution is the limiting phenomenon and the diffusion coefficient is infinite, (b) diffusion is the limiting phenomenon and the concentration at the interface is the saturation concentration, C^{s}_{liq}, and (c) both phenomena, dissolution and diffusion, are accounted for. δ denotes the diffusion boundary layer where most of the dissolved solute accumulates.

Table 1
Diffusion coefficients of Fe, Ni and Co atoms in liquid Al used in Eq. (5) [30].

Element	Pre-exponential factor, D_0 [m^2 s^{-1}]	Activation energy, Q [kJ mol^{-1} K^{-1}]
Fe	2.34×10^{-7}	35.0
Ni	9.54×10^{-8}	26.0
Co	8.13×10^{-8}	27.4

diffusive flux of the dissolved species near the interface is approximated by

$$\frac{dC_{liquid}}{dt} = \frac{D(\theta)}{\delta}(C_{int} - C_{bulk}) \tag{6}$$

where δ is the diffusion boundary layer and C_{bulk} is the nominal concentration in the liquid.

Following the assumptions of Verhaeghe et al. [28], three dissolution cases can arise. The cases are schematically represented in Fig. 3 with the evolution of the concentration adjacent to the interface and the profile of concentration in the bulk of the liquid. The cases are:

1) *Dissolution control*, Fig. 3(a): solid-to-liquid migration is the limiting factor, i.e. ${}^{D}/_{\delta} \gg K$. This case is also known as kinetic dissolution [31,32]. The diffusion coefficient is large enough to consider the homogeneous composition of the liquid. Therefore, the dissolution is controlled by the rate of migration of atoms from the IM to the liquid as modelled by Eq. (3). This is the case for systems where the ratio ${}^{S}/_{V}$ is very large;
2) *Diffusion control*, Fig. 3(b): diffusion is the limiting factor, i.e. ${}^{D}/_{\delta} \ll K$. In this case, owing to the low diffusivity of the dissolved species in the liquid, they accumulate at the interface. The latter quickly reaches the saturation concentration, $C_{int} = C^{s}_{liq}$, and only the Fick's second law (Eq. (4)) has to be solved;
3) *Dissolution-diffusion control*, Fig. 3(c): In the third case, the dissolution reaction kinetics and the diffusion rate of the solute within the liquid are similar. Both phenomena have to be accounted for to describe the dissolution process.

Due to the nature of the welding process, exhibiting short reaction times and large heating and cooling rates, the process has to be treated as transient, so that the third case is expected to apply. The 1-D second Fick's law of Eq. (4) is solved by imposing the dissolution flux of the species modelled by Eq. (3) as a Dirichlet boundary condition at the IM-liquid interface, i.e. $C_{liquid} = C_{int}$ at $x = 0$. On the opposite boundary, $x = L$, the flux of the diffusing species is set to zero.

In order to implement Eq. (3), the ratio ${}^{S}/_{V}$ that accounts for the dimensions of the dissolution problem is removed. The geometry of the molten pool is already accounted for in the Fick's diffusion law (Eq. (4)). Therefore, Eq. (3) becomes

$$\frac{dC_{int}}{dt} = k\left(C^{s}_{liq}(\theta) - C_{int}\right) \tag{7}$$

where $k = k^{*S}/_{V}$.

For the particular case of FMB, the reaction-diffusion problem is modelled with the following hypotheses:

1) The solute flow in the molten pool is modelled under pure diffusion conditions. The convective flows in the molten pool are thus neglected. Indeed, in the FMB welding process, the molten pool is not subjected to forced, thermal or electromagnetic convection. Only the Marangoni flow due to the non-homogeneous temperature and concentration gradients [33] might bring some convection but it is not accounted for here.
2) The solute diffusion in the solid is negligible compared to the diffusion in the liquid. According to Du et al. [30], the diffusion coefficient in liquid aluminium for the studied species, Fe, Ni and Co, is at least

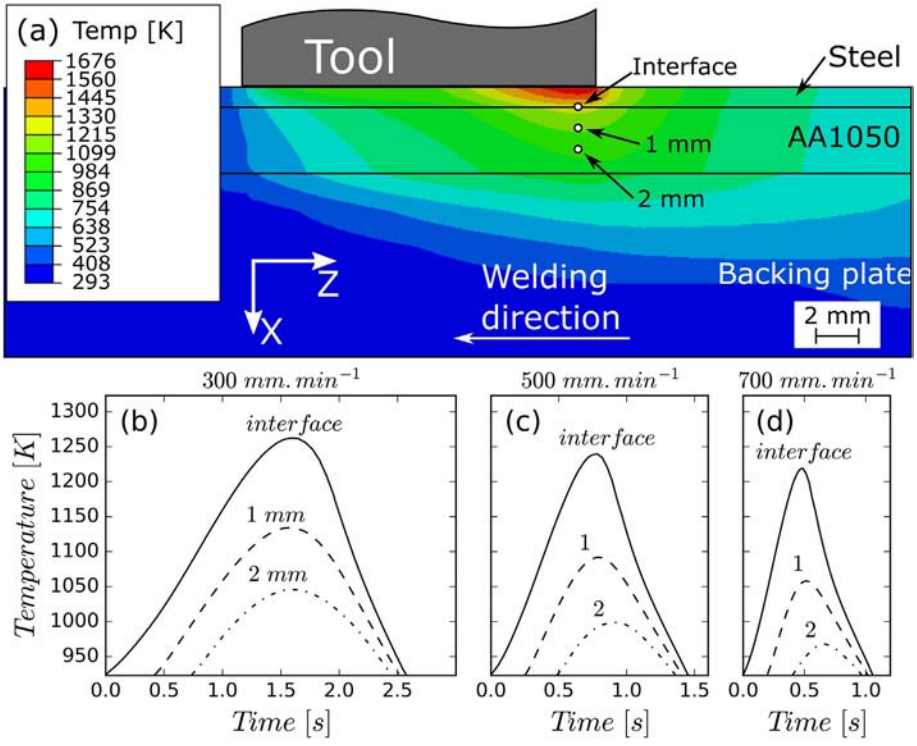

Fig. 4. (a) Longitudinal view of the heat-transfer simulation carried out with Abaqus [34] for a weld performed at 500 mm·min^{-1}. (b, c, d) Temperature at the centreline of the weld at three different distances from the interface (interface, 1 mm and 2 mm) from the simulations at 3 different welding speeds (b) 300, (c) 500 and (d) 700 mm·min^{-1}.

three orders of magnitude larger than in the solid. The diffusion coefficients in the solid are thus set to zero.
3) Despite the IM formation and dissolution phenomena, the interface does not move significantly compared to the length of the system and is thus considered as fixed.
4) Any delay in the reaction due to the presence of native oxide layers on the surface of the plates is neglected.

The model accounts for solute precipitation during solidification. When the temperature drops below the liquidus temperature, the concentration of the liquid is set to the new equilibrium concentration and the difference with the previous concentration corresponds to the precipitated solute. Since the cooling in FMB is monotonous, the precipitated solute does not further participate in the diffusion process.

The 1-D model to solve the second Fick's law (Eq. (4)) was implemented in Python using a finite difference method. The total length of the system was 2 mm, the element size was 2 μm and the time step was 0.004 s. The constants for diffusivity of the dissolved species (i.e. Fe, Ni or Co) of Eq. (5), provided in Table 1, have been obtained from the work of Du et al. [30]. The temperature of an element (used to calculate the diffusion coefficient in Eq. (5)) is calculated as the average temperature of the two nodes defining the element. The model requires the thermal cycle of each node. This one is assessed from a finite element (FE) heat transfer model described below.

3. Thermal modelling

The thermal fields during welding were simulated using a FE heat transfer model implemented in Abaqus [34] (Fig. 4(a)). The model is an adaptation of the model proposed by Crucifix et al. [12]. The aluminium and steel plates as well as the stainless steel backing plate are included in the model along with the welding table. The thermal conductivity and heat capacity of Dual-Phase steel plate are considered as the properties of pure iron [35–37]. Similarly, the thermal properties of the aluminium alloy AA1050 are considered as those of pure aluminium in both solid and liquid states [35]. The contact between the surfaces is divided into two regions with either high or low thermal gap conductances [12]. The high gap conductance value is arbitrarily chosen sufficiently high to ensure a temperature continuity between interfaces, i.e. 10^6 kW m^{-2} K^{-1}. Three regions are associated to this value: (i) the contact between the molten Al and the steel plate just below the tool; (ii) the contact between the Al plate and the backing plate just below the tool; and (iii) the welded regions due to the presence of a thin IM layer that suppresses the gap between the plates. Everywhere else, the contacts are assumed to present a low conductance value. Due to the similarity of the systems, the same value as assessed by Crucifix et al. [12] is used for the low conductivity contacts, i.e. 10 kW m^{-2} K^{-1}. The emissivity and convection coefficients at the surfaces exposed to the air are 0.3 and 15 W m^{-2} K^{-1}, respectively [38,39].

The model requires the power input, P, as a measurement of the energy introduced in the system [40]. P is inferred from in-situ torque measurements as follows:

$$P = \eta(T_z \omega) \tag{8}$$

where T_z is the torque, ω is the rotational speed, and $\eta \in [0,1]$ is the efficiency. The value of $\eta = 0.9$ is taken from the work of Crucifix et al. [12].

Table 2
Composition of the base materials measured by inductive coupled plasma (ICP).

Wt%	Al	Fe	Si	Ti	Mn	Ga	V	C	Cr
AA1050	Rest	0.38	0.06	0.01	0.01	0.01	0.01	–	–
DP600	0.02	Rest	0.21	0.02	1.96	–	–	0.16	0.19

Table 3
Process parameters and power input during welding with a constant rotational speed of 2000 rpm. The power input has been inferred from the torque measurements on the tool using Eq. (8).

Welding speed [mm·min^{-1}]	Tool plunge [mm]	Power input [kW]
300	−0.11	3.6 ± 0.1
500	−0.16	4.0 ± 0.2
700	−0.19	4.4 ± 0.1

The coated interlayers are not accounted for in the model due to their low thickness compared to the rest of the dimensions. The latent heat of the reaction between Al and Fe as well as the dissolution are also not considered in the thermal model, only the latent heat of fusion of aluminium is accounted for. This model has been validated in previous publications [12,14,21].

Fig. 4(a) shows the resulting simulated temperature distribution for welding performed at 500 mm·min^{-1}. Fig. 4(b, c and d) shows the thermal cycles of the liquid aluminium at the weld centreline at different distances from the interface into the molten pool (interface, 1 mm and 2 mm) for welding speeds of 300, 500 and 700 mm·min^{-1}, respectively, and constant rotational speed of the tool of 2000 rpm.

4. Hot tearing assessment

Kou [23] demonstrated that the occurrence of hot tearing is proportional to $\left|{}^{\theta}/_{\sqrt{f_s(\theta)}}\right|$, where θ is the temperature and $f_s(\theta)$ is the solid fraction. He proposed a hot tearing risk (HTR) index as the maximum slope of the $\theta - \sqrt{f_s(\theta)}$ curve within a susceptibility interval of solid fraction between 0.84 and 0.98. Therefore, the HTR index is defined as [23]:

$$HTR = \max\left(\left|{}^{d\theta}/_{d\sqrt{f_s(\theta)}}\right|\right)_{0.84 \le f_s \le 0.98} \tag{9}$$

To evaluate the HTR index, the solidification path of the alloy has to be known. The $f_s(\theta)$ curve for the studied compositions was calculated using the Scheil-Gulliver module for non-equilibrium solidification in Thermocalc [41]. For the sake of simplicity, the welds without interlayer are analysed as a binary Fe-Al system [42] and no other impurities are accounted for. In the welds with nickel or cobalt interlayers, only Fe is accounted for as an impurity (0.38 wt%, Table 2) so that they are thus analysed as Ni-Fe-Al and Co-Fe-Al ternary systems, respectively [43].

5. Experimental methods

The base materials were commercially pure aluminium alloy AA1050 and Dual-Phase steel (DP600), with thicknesses of 3 and 0.9 mm, respectively. The compositions are provided in Table 2. The as-received plates were machined to dimensions of 200 × 80 mm. The surface of the plates was ground with a 320-grit abrasive paper and cleaned with acetone. The stack was completed with a stainless steel backing plate below the aluminium plate to protect the welding plate and to minimise the heat losses through the bottom of the stack. The welds were performed on a Hermle milling machine. The welding tool was a 16-mm diameter cemented tungsten carbide cylinder. The tool had a backwards angle of 0.5° and the rotational speed was set to

Table 4
Composition of the electroplating baths for Ni and Co [44,45].

Ni plating		Co plating	
Reactive	Concentration [g l^{-1}]	Reactive	Concentration [g l^{-1}]
$NiSO_4 \cdot 6H_2O$	50	$CoSO_4 \cdot 7H_2O$	400
$NiCl_2 \cdot 6H_2O$	30	NaCl	17
H_3BO_3	30	H_3BO_3	45

Table 5
Parameters for electroplating [44,45].

	Ni Plating	Co plating
Temperature [°C]	55	25
Current density [A cm^{-2}]	4.2×10^{-2}	4.2×10^{-2}
Time [s]	720	370

2000 rpm. The plunge of the tool into the steel, provided in Table 3, was increased with the welding speed to ensure a good contact between the tool and the steel plate. The welding speeds were set to 300, 500 and 700 mm·min^{-1}, respectively. Three welds per welding speed and interlayer were performed. The power input, provided in Table 3, was inferred from torque measurements performed with a Kistler dynamometer using Eq. (8).

The Ni and Co plating were performed on the steel plate using the solutions provided in Table 4 and the parameters in Table 5 [44,45]. To increase the performance of the deposition, the areas to be coated were delimited with adhesive tape. The thickness of the plating was calculated as the total weight gain after plating divided by plated area and density of the plated element. This assessment yielded approximately 5 μm for Co and 10 μm for Ni. Three systems are labelled according to the main element in contact with the liquid aluminium: Fe-Al system for the weld without interlayer and Ni-Al and Co-Al systems for those performed with nickel and cobalt interlayers, respectively.

The dissolved solutes in the molten pool were measured by EDX at different distances from the interface at the weld centreline. The measurements were performed on horizontal rectangles of 125×10 μm^2. The long side of this rectangle was parallel to the interface in order to average horizontally the variations in composition resulting from microsegregation.

6. Results

The SEM observations in this section reveal the reduction of IM thickness achieved with the use of Co and Ni interlayers as well as the detection of hot tears just below the welded interface. The dissolution of the interlayer in the molten pool is also revealed with SEM observations while the concentration of dissolved species in the aluminium plate is measured using EDX at different distances from the interface. Then, the dissolution model is used along with the thermal profiles assessed from the finite element model to fit the value of the dissolution rate, *k*. Finally, the hot tearing susceptibility of AA1050 after dissolution of the interlayer is assessed for the range of compositions observed.

6.1. SEM observation

Fig. 5 shows welds where only half of the welded surface was previously coated, while the other half surface shows the direct Fe-Al reaction for reference. In both cases of Ni and Co interlayers, the IM layer is thinner. As observed in Fig. 5(a), the thickness of the IM layer formed in the Ni-plated region is 0.7 ± 0.1 μm while the IM layer in the non-plated region is 6.9 ± 1.0 μm. In the case for the Co plating shown in Fig. 5(b), the thickness of the IM layer below the Co-plated region is 2.2 ± 0.2 μm while it is 6.4 ± 0.5 μm in the non-plated region.

Fig. 6(a, b and c) corresponds to SEM micrographs of the solidified pool just below the interface at the weld centreline for the Fe-Al, Ni-Al and Co-Al systems, respectively, for a welding speed of 300 mm·min^{-1}. It can be observed that the microstructure changes with the welding system. The Fe-Al system in Fig. 6(a) presents primary Al grains surrounded by an eutectic phase. In the case of the Ni plated system, Ni-Al needle-shaped precipitates surrounded by a eutectic phase can be observed as indicated by the white arrow in Fig. 6(b). This microstructure suggests that, during welding, the molten pool presented Ni concentrations above the eutectic concentration. For the Co-Al system, a eutectic dominated microstructure can be observed close to the interface, highlighted by the white arrow in Fig. 6(c). Further away from the interface, the microstructure is mostly composed of the Al phase surrounded by a eutectic phase.

Fig. 7(a, b and c) provides the EDX measurements of the dissolving species performed on Fig. 6(a, b and c), respectively. The measurements are performed at increasing distances from the reaction interface. It can be observed that the concentration of the dissolving species (Fe, Ni and Co, respectively) decreases as the distance to the interface increases. The EDX measurements also reveal that the concentration of dissolved species is lower as the welding speed increases for the three reactive systems.

Hot tears are found in the Ni-Al system for every welding speed (Fig. 8(a)) and for the Co-Al system for a welding speed of 700 mm·min^{-1} (Fig. 8(b)). No hot tears were observed in the Fe-Al system. The dissolution of the interlayer thus seems to modify the solidification behaviour of the aluminium, increasing the hot tearing occurrence.

6.2. Interface dissolution in liquid Al

In order to validate the hypothesis described in Section 2 stating that the convective fluxes (i.e. Marangoni flux) are negligible and the dissolved species flow under pure diffusion conditions in the molten pool, cross sections of the welds with Ni plating performed at 300 and 500 mm.min^{-1} were examined by SEM. The EDX maps shown in Fig. 9 reveal the distribution of the dissolved Ni in the molten pool. At a welding speed of 300 mm·min^{-1}, Fig. 9(a), a Ni-rich area (in red) is found in the bulk of the aluminium molten pool (in black). This Ni-rich area is associated to the presence of convective fluxes. At a welding speed of 500 mm·min^{-1}, all the dissolved Ni (in red) is found close to the interface in a diffusion layer of about 300 μm thick between the steel plate (in blue) and the aluminium plate (in black). No Ni-rich areas are observed anywhere else in the pool (Fig. 9(b)). These observations also prevail for a Ni-plated weld performed at 700 mm·min^{-1}.

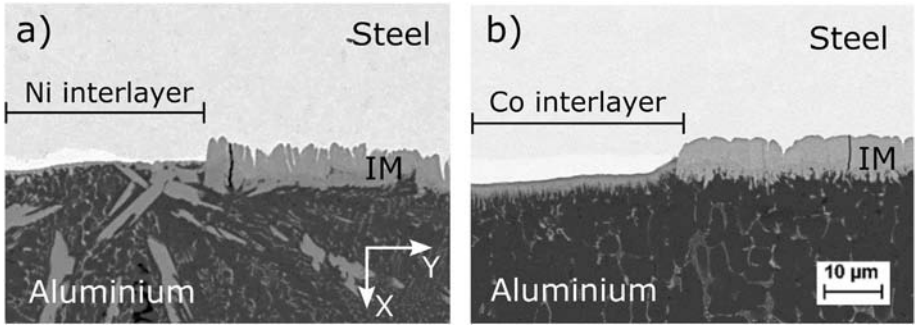

Fig. 5. SEM observations of the interfaces after welding, illustrating the thickness reduction achieved with (a) a Ni interlayer and (b) a Co interlayer. The left sides of the micrographs show the coated interface while the right sides show the uncoated interface for reference.

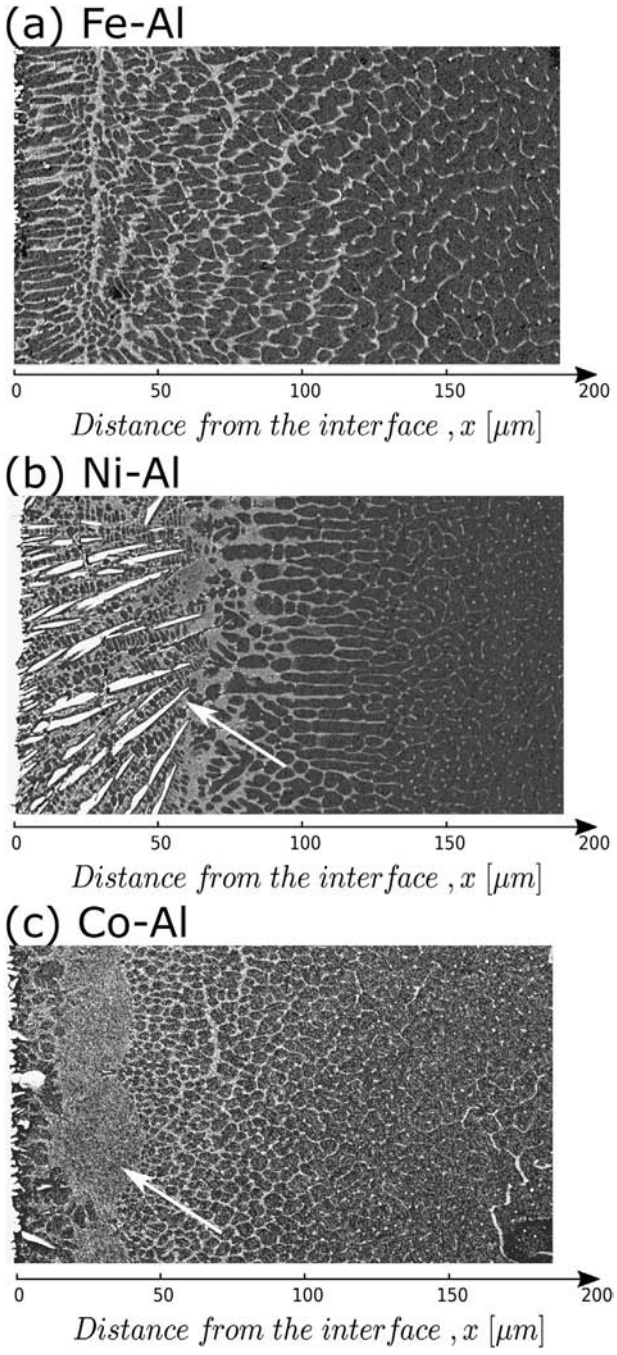

Fig. 6. Backscatter SEM observations with backscattered electrons of the solidified aluminium just below the interface for (a) Fe-Al, (b) Ni-Al and (c) Co-Al systems, respectively, at a welding speed of 300 mm·min^{-1}. The white arrow in (b) shows the needle-shaped precipitates. The white arrow in (c) shows the eutectic microstructure.

The continuous lines in Fig. 7(a, b and c) correspond to the fitted diffusion profiles of the dissolving species using the finite differences model described in Section 2, the temperatures from the FE model from Fig. 4 and the fitted values of k for Eq. (7) provided in Table 6. The fitting of k has been carried out using a least squares procedure constrained by the area below the curves, i.e. the area of the fitted profiles should equal the area below the curve defined by the experimental measurements. The welds performed at 500 and 700 mm·min^{-1} were used for fitting since they are compliant with the pure diffusion hypothesis described in Section 2 and no convective fluxes were observed. Besides a general good agreement, the differences in solute distribution between the experiments and the model can be explained by the macrosegregation owing to a transient solidification front that increases the solute concentration at the latest stages of solidification [46]. The lowest solute concentrations in the molten pool are found for the Co-Al system, while the largest concentrations are found for the Ni-Al system.

6.3. Hot tearing risk

The occurrence of the hot tearing during the solidification of the molten pool owing to the dissolution of the interface is assessed by evaluating Eq. (9) for the composition profiles represented in Fig. 7(a, b and c). The $\theta - \sqrt{f_s(\theta)}$ curves for a selected range of Ni and Co concentrations are shown in Fig. 10. These curves include the presence of iron impurities, so that, they are treated as ternary systems. The dashed straight lines show the maximum slope within the susceptibility interval. It can be observed that the risk is maximum at low concentrations, i.e. around 0.08 at.% of Ni and 0.01 at.% of Co in the Ni-Al and Co-Al systems, respectively. The curves of the Fe-Al system are not shown since they are flat in the susceptibility range, confirming the experimental observation that the HTR in the analysed interval of compositions is zero. Fig. 11 shows the HTR index as a function of the Ni and Co concentrations, respectively.

7. Discussion

The Al to steel welding brings 2 potential challenges for the integrity of the joint, i.e., the formation of a brittle IM layer and the hot tearing

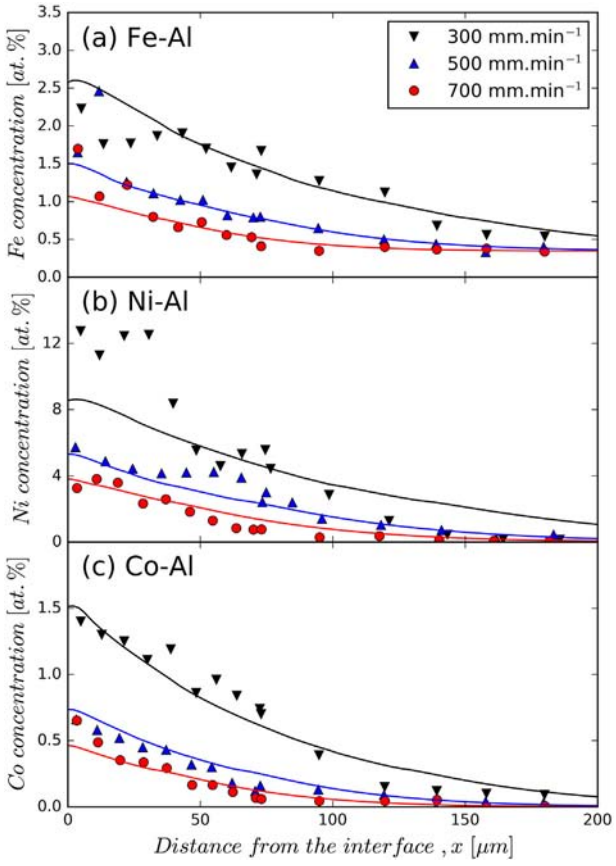

Fig. 7. Concentration profiles of the dissolved species in the re-solidified Al shown in Fig. 6 as a function of the distance from the interface for the (a) Fe-Al, (b) Ni-Al and (c) Co-Al systems, respectively. The points represent the measurements performed by EDX. The continuous lines correspond to the simulated profiles. The measurements and simulations have been carried out for the three studied welding speeds. It is worth emphasizing the different scales for the concentration.

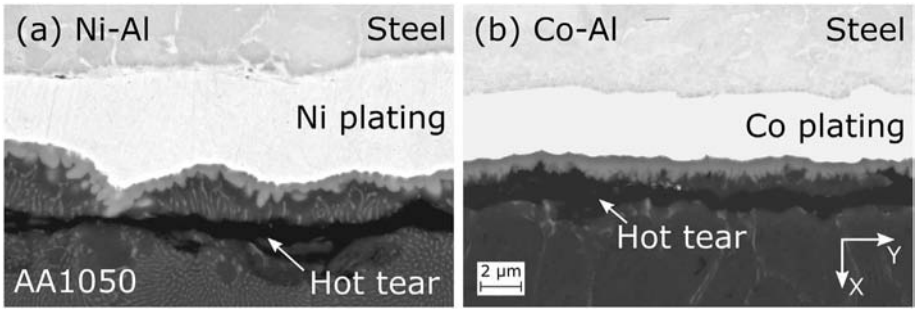

Fig. 8. SEM observations of the hot tears formed in the solidified aluminium during the solidification process for (a) a Ni interlayer and (b) a Co interlayer. Large hot tears are found at all welding speeds with a Ni interlayer. The hot tears in the case of a Co interlayer are much smaller and their occurrence is restricted to welds performed at 700 mm·min^{-1}.

appearance. An additional layer seems very effective to reduce the thickness of the IM layer and to increase the strength of the Al-to-steel weld as previously demonstrated by Reddy et al. [7] and Jimenez-Mena et al. [14]. Nevertheless, an increase of hot tearing susceptibility can occur because of the dissolving interlayer. Thus, in order to predict the potential strength increase that an interlayer can bring, an integrated approach of the problem is suggested. First, the thermal model developed by Crucifix et al. [12] allows predicting the thermal cycles that can result in a control of the IM layer thickness. Also, the resulting thermomechanical cycles can influence the formation of hot tears [21] or residual stresses [47]. Then, the nature of the interlayer is chosen using two criteria (i) Assessing the IM layer thickness reduction that it will bring as shown in the work of Jimenez-Mena et al. [14], and (ii) evaluating the impact that the interlayer will have in the hot tear susceptibility of the aluminium alloy as described in this work.

The following sections discuss the methodology to evaluate such impact in hot tear susceptibility. First, the performance of the kinetic dissolution model to predict the dissolution of the interface in purely diffusive systems is first discussed. Then, the predictions of Kou's model for the hot tearing susceptibility [23] owing to the dissolution of the interface are then compared to the experiments. Finally, a criterion to choose an interlayer based on the dissolution rate and the hot tear susceptibility is discussed and potential materials for interlayers are suggested.

7.1. Dissolution of the interface

The dissolution behaviour of the interface in the liquid aluminium has been modelled combining a kinetic dissolution boundary at the interface and pure diffusion of the dissolving species in the molten pool (Eqs. (3) and (4), respectively). The kinetic behaviour of an interface has been often defined as the combination of the intrinsic dissolution rate and the geometry of the dissolving system using a constant $k = k^* \cdot {}^{S}/_{V}$. In the model proposed in this work, the geometry of the system is not accounted for since it is already accounted for in the finite differences model for diffusion of the dissolved species in the molten pool.

Yeremenko et al. [48] calculated $k^* \cdot {}^{S}/_{V} = 0.38 \times 10^{-3}\ s^{-1}$ for the dissolution of pure iron in liquid pure aluminium, which is three orders of magnitude lower than the value calculated in this work, $k = 0.37\ s^{-1}$. The difference is mainly explained by the fact that Yeremenko et al. [48] based their calculations in the case described in Fig. 3(a) by considering a homogeneous concentration in the liquid aluminium. In this work, k was assessed using the case described in Fig. 3(c), which requires to know the concentration profile in the liquid aluminium. Dybkov [49] used a similar system to the one used by Yeremenko et al. [48] to measure the dissolution of Fe-Ni alloys in liquid aluminium at different concentrations and rotational speeds of the sample in the liquid aluminium in order to change the hydrodynamic boundary which modifies as well the diffusion boundary, δ. They observed that the value of $k^* \cdot {}^{S}/_{V}$ depends on the rotational speed, what implies that k^* is a property of the experimental conditions and not only of the chemical properties of the metals in contact. In the present work, the dissolutive behaviour of Eq. (7) is a boundary condition of the whole system, which makes it independent of the flow (either convective or diffusive) of the dissolved species in the liquid aluminium. Therefore, k only represents the chemistry of the contact and could be used as input data in further models.

The evolution of the concentration of the dissolving species at the interface as a function of time is shown in Fig. 12 for the three systems at a

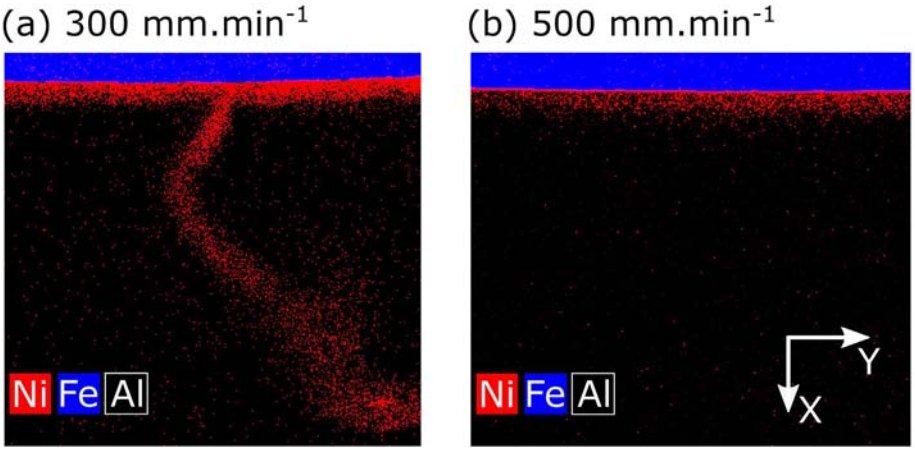

Fig. 9. EDX mapping of Ni-Al system welds performed at (a) 300 mm·min^{-1} and (b) 500 mm·min^{-1}. The blue, black and red colours correspond to Fe, Al and Ni, respectively. At slow welding speed, (a), Ni-rich areas can be found in the bulk of the molten pool owing to the convection inside. At faster welding speeds, (b), the Ni stays close to the surface in the diffusion boundary.

Table 6
Fitted values of k from Eq. (7).

System	k (s^{-1})
Fe-Al	0.38
Ni-Al	0.37
Co-Al	0.17

constant temperature of 900 °C. The profiles of Fig. 12 suggest that the dissolution of the interface is mainly dominated by the solubility of the dissolving species in liquid aluminium, C^{s}_{liq}, at long reaction times. This can be observed when comparing the curves of Fe and Ni in Fig. 12. Indeed, Fe and Ni show similar values of k, 0.38 and 0.37 s^{-1}, respectively, but the concentration at the interface increases much faster in the case of Ni since its solubility in liquid Al at 900 °C is about 3 times larger than the one of Fe, 5.3 and 16.3 at.%, respectively (Table 7). When the values of solubility are similar, as in the case of Fe and Co, 5.3 and 5.4 at.%, respectively, the value of k then determines the concentration at the interface. The value of k for Fe in liquid aluminium is roughly twice the value of Co, 0.38 and 0.17 s^{-1}, respectively. In this case, two time scales can be observed on Fig. 12. If the dissolution process is of the order of a few seconds, notably below 15 s, the process is in a transient state where the dissolution of Fe is faster. On the other hand, if the dissolution time is much longer than 15 s, the interface reaches the saturation concentration. As shown in Fig. 4(b, c and d), dissolution only lasts for around 2 s, which well justifies the transient nature of the process.

The Ni-rich areas in the bulk of the molten pool (Fig. 9(a)) indicate that the pure diffusion hypothesis is not met for a welding speed of 300 mm·min^{-1}. Those Ni-rich areas are the result of convective fluxes that displace the dissolved species from the dissolution boundary layer to the bulk of the molten pool. With the presence of convective fluxes, the migration of the dissolving species cannot be modelled exclusively with a Fick's diffusion law and the liquid flow in the molten pool should also be accounted for. On the other hand, welds performed at 500 and 700 mm·min^{-1} show no convective fluxes since no Ni is found away from the diffusion boundary layer (Fig. 9(b)). Hence, the samples met the hypothesis described in Section 2. It is worth noting that, despite the presence of convective fluxes, the model captures quite well the solute profile in the aluminium at a welding speed of 300 mm·min^{-1}. Since the measurements were taken at the weld centreline, it is suggested that the convective fluxes are low at this point owing to the symmetry of the system.

The thickness of the interlayer that has been dissolved can be calculated by integrating the concentration of the dissolved species in the molten pool and dividing by the density of the element (Fe, Ni or Co). The dissolved thickness for a weld performed at 300 mm·min^{-1} is 1.3, 7.2 and 0.7 μm for Fe, Ni and Co, respectively. The minimum plating thickness in the case of Ni should therefore be approximately ten times larger than in the case of Co to avoid its complete dissolution. This has an impact on the cost of the process since more solute, energy and time are needed to perform the coating.

The solubility of metals can be used as a first-order criterion to choose the interlayer. Table 7 suggests several candidates, with higher melting temperatures than Al, according to the maximum solubility at 900 °C [3]. The best elements to reduce the dissolution of the interlayer are those with the lower values of C^{s}_{liq}. Ti and Mo could thus be good candidates. On the other hand, Cu and Ag, as used in the work of Reddy et al. [7], show a large solubility in liquid Al and the interlayer would quickly dissolve in the molten pool. Therefore, Ag and Cu, which were good alternatives in solid state welding, are not suitable in reactive wetting welding unless very thick interlayers are deposited.

7.2. Effect of dissolution on the IM growth

According to Tanaka et al. [4], an IM thickness below 1 μm is necessary to increase the strength of the welded interface. As observed in Fig. 5(a), the use of a Ni interlayer provides a 90% reduction of the IM layer thickness compared to a weld without interlayer. The IM thicknesses reported in literature for some of the most common reactive wetting welding processes such as arc-welding or resistance welding are roughly between 4 and 15 μm [5,9,13]. Disregarding the effect of the nature of the IM compound, the use of a Ni interlayer would be sufficient to achieve thicknesses in the order of 1 μm for most reported cases and potentially increase the toughness of the weld. On the other hand, the Co interlayer provides a 65% reduction in the IM thickness and would be mostly interesting in welds where the original IM thickness is around 3 μm.

The growth rate of the IM layer is the result of a competition between the formation reaction and the dissolution in the molten pool as explained by Tanaka et al. [19]. The thick IM layer formed in the Fe-Al system results from the combination of a low dissolution rate of the iron aluminides in the liquid aluminium and a high reaction rate.

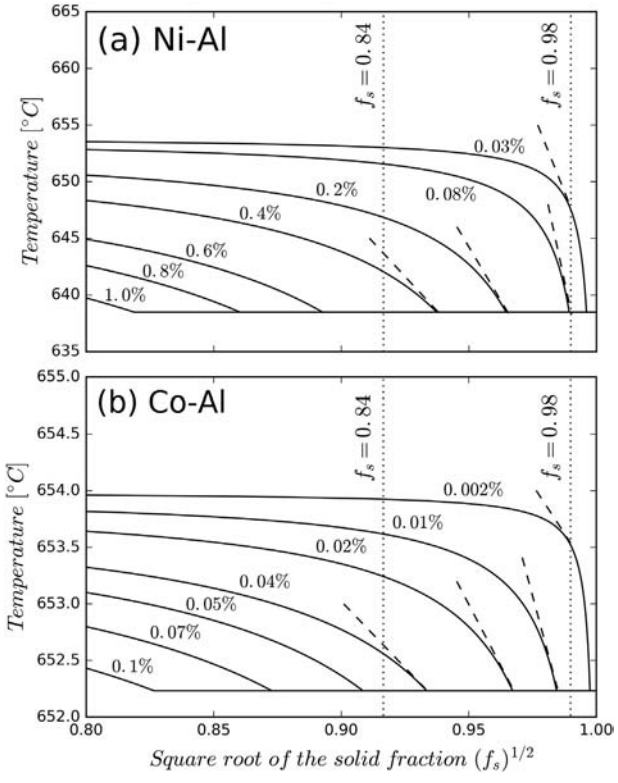

Fig. 10. $\theta - \sqrt{f_s(\theta)}$ curves allowing the estimation of the risk of hot tearing in the (a) Ni-Al system and (b) Co-Al system. The curves have been calculated using the Scheil module in Thermocalc [41]. The dashed lines show the maximum slope of the curves in the susceptibility interval according to Kou's criterion (Eq. (9)) [23]. It is worth emphasizing the different temperature scales.

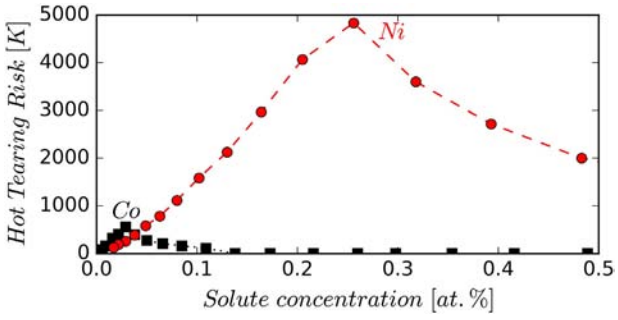

Fig. 11. Hot tearing risk (HTR) index from Eq. (9) as a function of concentration for the Ni-Al and Co-Al systems for a welding speed of 500 mm·min^{-1}.

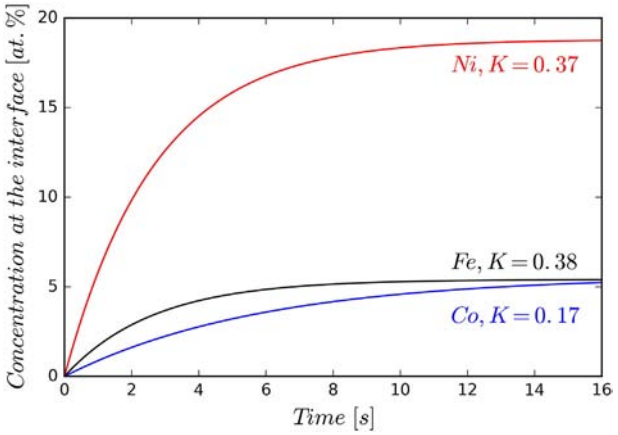

Fig. 12. Concentration of the studied elements at the interface as a function of time using Eq. (7) and the fitted values of k in Table 6 for a constant temperature of 900 °C.

Owing to the low dissolution rate of the cobalt aluminides in the liquid aluminium, the thinner IM layer formed in the Co-Al system can be only explained by the low reaction rates between the Co and the steel. In the case of the Ni-Al system, the large dissolution rates control the IM layer growth. The reaction rates for the formation of the Ni/Al IM layer are therefore similar to the dissolution rates, keeping the thickness of the IM layer at a minimum.

7.3. Hot tearing prediction

The dissolved species change the solidification behaviour of the aluminium molten pool. Hence, hot tears and solidification shrinkage can arise as solidification defects. The presence of hot tears results in a degradation of the mechanical properties of the joint [5]. Kou's criterion [23] to predict the formation of hot tears provides a semi-quantitative comparison of the susceptibility of alloys to form hot tears with regard to their composition.

Fig. 11 shows that the HTR index quantifying the hot tearing susceptibility, i.e., the maximum slope of the curves in the susceptibility range, is larger at low solute concentrations with respect to the maximum solubility of the dissolved species. The larger HTR values for the Ni-Al system confirm the observations that the Ni-Al system is much more prone to hot tears than the Co-Al system (Fig. 11). This criterion also correctly predicts the lack of formation of hot tears for the Fe-Al system. The Fe concentration in the base material is 0.38 wt%, a concentration that shows no susceptibility to hot tearing and neither does any higher Fe concentration. The HTR is maximum at low concentration of the dissolving species, in the order of 0.1 and 0.01 at.% for Ni and Co, respectively. Such low concentrations of dissolved Ni or Co bring, even for short dissolution time, a significant increase of the hot tear susceptibility of AA1050.

Unlike the RDG criterion [24], Kou's criterion [23] depends solely on the composition of the alloy, the effect of the welding speed on the maximum HTR index cannot be predicted. However, the formation of hot tears only for a welding speed of 700 mm·min^{-1} in the Co-Al system indicates that there is indeed an effect of this welding speed. Crucifix et al. [12] observed that the amount of hot tears increased with increasing welding speed. In the case of the Ni-Al system, owing to its large HTR index, hot tears are found for every welding speed. In the case of Co, due to its lower susceptibility, hot tears are only found if the thermomechanical cycles meet the conditions for the formation of hot tears. These conditions are met for large welding speeds [5,12,21]. In further analyses, other impurities such as Si or Cu could be accounted for and included in the Scheil-Gulliver calculations.

In the present work, AA1050 is an alloy presenting a large resistance to hot tearing which has been hindered by the dissolution of the interlayer. However, the opposite case can be considered: an alloy prone to hot tearing that becomes less susceptible due to the dissolution of an interlayer. It could be the case for AA2024 alloy, which has been observed to be prone to hot tearing [5,12]. A similar concept is already used in aluminium arc welding, where an Al-Si filler material is mixed with the welded alloy in the molten pool, suppressing the formation of hot tears by changing the composition [50,51]. In that case, an interlayer material with a high solubility, such as Si, Cu or Ag (Table 7) could be considered. The case of Si is particularly interesting since it is known to reduce hot tear susceptibility when added to an aluminium alloy [51]. Furthermore, Si does not form IM phases with Al. Also, if the Si interlayer completely dissolves and leaves the steel plate in contact with the liquid aluminium, the presence of dissolved Si in the liquid aluminium reduces the growth rate of the Fe-Al IM layer [52].

Furthermore, the choice of the aluminium alloy to be welded might constraint the choice of the interlayer. In this work, AA1050 drastically changes its hot tearing susceptibility with the dissolution of small amounts of Ni. It would be worth studying base materials with compositions that remain resistant to hot tearing even though part of the interlayer is dissolved into the molten pool.

Table 7
Maximum solubility, in liquid aluminium at 900 °C, of candidate materials according to the equilibrium phase diagram [3].

Element	Saturation concentration, C^{*}_{liq} [at.%]
Ti	0.80
Mo	0.85
Cr	4.2
Fe	5.3
Co	5.4
Ni	16.3
Cu	55.3
Ag	91.3

8. Conclusions

A methodology to choose an interlayer to control the IM thickness in dissimilar steel-to-aluminium welding by Friction Melt Bonding has been developed. Ni and Co are good candidates since their use as interlayer significantly reduces the thickness of the IM layer. However, in addition to their potential to control the IM thickness, two phenomena have to be accounted for when choosing the interlayer, the dissolution rate of the interlayer in the Al molten pool and the changes induced in the solidification behaviour of the molten pool potentially leading to hot tearing.

The dissolution of the interface and subsequent diffusion of the dissolved species in liquid Al has been modelled using the second Fick's law in a purely diffusive model if the convective fluxes in the molten pool are low. At the solid-liquid interface, a kinetic dissolution behaviour has been imposed as boundary condition to capture the behaviour of the interface during dissolution and the value of the dissolution reaction rate, k, has been fitted.

The risk of formation of hot tears has been assessed using the Scheil-Gulliver equation and the hot tearing criterion developed by Kou [23]. The criterion can predict the risk of hot tearing formation quantified in a hot tearing risk (HTR) index. The criterion predicts correctly the formation of hot tears when using Ni and Co coatings. It also predicts the absence of hot tears for welds performed without interlayer. The highest risk of hot tearing formation is found at low solute concentrations.

Data availability

All data processed herein are available on request.

CRediT authorship contribution statement

N. Jimenez-Mena: Conceptualization, Investigation, Formal analysis, Writing - original draft. **A. Simar:** Conceptualization, Supervision, Writing - review & editing, Validation. **P.J. Jacques:** Conceptualization, Supervision, Writing - review & editing, Validation.

Declaration of Competing Interest

None.

Acknowledgements

N. Jimenez-Mena acknowledges the financial support of FRIA, Belgium. AS acknowledges the financial support of the European Research Council for a starting grant under grant agreement 716678, ALUFIX project.

References

[1] U. Dilthey, L. Stein, Multimaterial car body design: challenge for welding and joining, Sci. Technol. Weld. Join. 11 (2006) 135–142.
[2] X. Cui, H. Zhang, S. Wang, L. Zhang, J. Ko, Design of lightweight multi-material automotive bodies using new material performance indices of thin-walled beams for the material selection with crashworthiness consideration, Mater. Des. 32 (2011) 815–821.
[3] T.B. Massalski, J. Murray, Binary Phase Diagrams, ASM International, 1990.
[4] T. Tanaka, T. Morishige, T. Hirata, Comprehensive analysis of joint strength for dissimilar friction stir welds of mild steel to aluminum alloys, Scr. Mater. 61 (2009) 756–759.
[5] C. van der Rest, P.J. Jacques, A. Simar, On the joining of steel and aluminium by means of a new friction melt bonding process, Scr. Mater. 77 (2014) 25–28.
[6] A. Simar, M.-N. Avettand-Fènoël, State of the art about dissimilar metal friction stir welding, Sci. Technol. Weld. Join. 22 (2016) 389–403.
[7] M.G. Reddy, S.A. Rao, T. Mohandas, Role of electroplated interlayer in continuous drive friction welding of AA6061 to AISI 304 dissimilar metals, Sci. Technol. Weld. Join. 13 (2008) 619–628.
[8] H. Dong, W. Hu, Y. Duan, X. Wang, C. Dong, Dissimilar metal joining of aluminum alloy to galvanized steel with Al–Si, Al–Cu, Al–Si–Cu and Zn–Al filler wires, J. Mater. Process. Technol. 212 (2012) 458–464.
[9] P. Peyre, G. Sierra, F. Deschaux-Beaume, D. Stuart, G. Fras, Generation of aluminium–steel joints with laser-induced reactive wetting, Mater. Sci. Eng. A 444 (2007) 327–338.
[10] R. Borrisutthekul, T. Yachi, Y. Miyashita, Y. Mutoh, Suppression of intermetallic reaction layer formation by controlling heat flow in dissimilar joining of steel and aluminum alloy, Mater. Sci. Eng. A 467 (2007) 108–113.
[11] M. Winnicki, A. Ma\lachowska, M. Korzeniowski, M. Jasiorski, A. Baszczuk, Aluminium to steel resistance spot welding with cold sprayed interlayer, Surf. Eng. 34 (2018) 235–242.
[12] S. Crucifix, C. van der Rest, N. Jimenez-Mena, P. Jacques, A. Simar, Modelling thermal cycles and intermetallic growth during friction melt bonding of ULC steel to aluminium alloy 2024-T3, Sci. Technol. Weld. Join. 20 (2015) 319–324.
[13] J. Fan, C. Thomy, F. Vollertsen, Effect of thermal cycle on the formation of intermetallic compounds in laser welding of aluminum-steel overlap joints, Phys. Procedia 12 (2011) 134–141.
[14] N. Jimenez-Mena, P.J. Jacques, L. Ding, N. Gauquelin, D. Schryvers, H. Idrissi, F. Delannay, A. Simar, Enhancement of toughness of Al-to-steel friction melt bonded welds via metallic interlayers, Mater. Sci. Eng. A 740–741 (2018) 274–284.
[15] P. Kannan, K. Balamurugan, K. Thirunavukkarasu, Influence of silver interlayer in dissimilar 6061-T6 aluminum MMC and AISI 304 stainless steel friction welds, Int. J. Adv. Manuf. Technol. 81 (2015) 1743–1756.
[16] S. Chen, Z. Zhai, J. Huang, X. Zhao, J. Xiong, Interface microstructure and fracture behavior of single/dual-beam laser welded steel-Al dissimilar joint produced with copper interlayer, Int. J. Adv. Manuf. Technol. 82 (2016) 631, https://doi.org/10.1007/s00170-015-7390-x.
[17] S. Chen, J. Huang, K. Ma, H. Zhang, X. Zhao, Influence of a Ni-foil interlayer on Fe/Al dissimilar joint by laser penetration welding, Mater. Lett. 79 (2012) 296–299.
[18] M. Yan, Z. Fan, Review durability of materials in molten aluminum alloys, J. Mater. Sci. 36 (2001) 285–295.
[19] Y. Tanaka, M. Kajihara, Kinetics of isothermal reactive diffusion between solid Fe and liquid Al, J. Mater. Sci. 45 (2010) 5676–5684.
[20] C.V.D. Rest, A. Simar, P.J. Jacques, Method for welding at least two layers (patent), International Publication No. WO2013164294 (A1), International Publication Date: 7 November, 2013., n.d.
[21] N. Jimenez-Mena, P. Jacques, J.-M. Drezet, A. Simar, On the prediction of hot tearing in Al-to-steel welding by friction melt bonding, Metall. Mater. Trans. A. 49 (2018) 2692–2704.
[22] D. Eskin, L. Katgerman, et al., Mechanical properties in the semi-solid state and hot tearing of aluminium alloys, Prog. Mater. Sci. 49 (2004) 629–711.
[23] S. Kou, A criterion for cracking during solidification, Acta Mater. 88 (2015) 366–374.
[24] M. Rappaz, J.-M. Drezet, M. Gremaud, A new hot-tearing criterion, Metall. Mater. Trans. A. 30 (1999) 449–455.
[25] T. Heumann, N. Dittrich, Structure character of the Fe2Al5 intermetallics compound in hot dip aluminizing process, Z. Met. 50 (1959) 617–623.
[26] A. Bouayad, C. Gerometta, A. Belkebir, A. Ambari, Kinetic interactions between solid iron and molten aluminium, Mater. Sci. Eng. A 363 (2003) 53–61.
[27] T. Sapanathan, N. Jimenez-Mena, I. Sabirov, M.A. Monclús, J.M. Molina-Aldareguia, P. Xia, L. Zhao, A. Simar, A new physical simulation tool to predict the interface of dissimilar aluminum to steel welds performed by friction melt bonding, J. Mater. Sci. Technol. (2019)https://doi.org/10.1016/j.jmst.2019.05.004.
[28] F. Verhaeghe, S. Arnout, B. Blanpain, P. Wollants, Lattice-Boltzmann modeling of dissolution phenomena, Phys. Rev. E 73 (2006), 036316.
[29] N. Tunca, G. Delamore, R. Smith, Corrosion of Mo, Nb, Cr, and Y in molten aluminum, Metall. Mater. Trans. A. 21 (1990) 2919–2928.
[30] Y. Du, Y. Chang, B. Huang, W. Gong, Z. Jin, H. Xu, Z. Yuan, Y. Liu, Y. He, F.-Y. Xie, Diffusion coefficients of some solutes in FCC and liquid Al: critical evaluation and correlation, Mater. Sci. Eng. A 363 (2003) 140–151.
[31] J. Zhang, P. Hosemann, S. Maloy, Models of liquid metal corrosion, J. Nucl. Mater. 404 (2010) 82–96.
[32] V. Yeremenko, Y.V. Natanzon, Kinetics of external dissolution of metals in metallic melts, Powder Metall. Met. Ceram. 9 (1970) 645–658.
[33] S. Kou, Welding Metallurgy, John Wiley & Sons, New Jersey, USA, 2003.
[34] Dassault-Systems, ABAQUS 6.14 Documentation, 2015.
[35] R. Powell, C.Y. Ho, P.E. Liley, Thermal Conductivity of Selected Materials, National standard reference data system 1966.
[36] P.D. Desai, Thermodynamic properties of iron and silicon, J. Phys. Chem. Ref. Data 15 (1986) 967–983.
[37] M. Li, J. Brooks, D. Atteridge, W. Porter, Thermophysical property measurements on low alloy high strength carbon steels, Scr. Mater. 36 (1997) 1353–1359.
[38] A. Bejan, A.D. Kraus, Heat Transfer Handbook, John Wiley & Sons, New Jersey, USA, 2003.
[39] W.M. Rohsenow, J.P. Hartnett, Y.I. Cho, et al., Handbook of Heat Transfer, McGraw-Hill, New York, USA, 1998.
[40] A. Simar, J. Lecomte-Beckers, T. Pardoen, B. De Meester, Effect of boundary conditions and heat source distribution on temperature distribution in friction stir welding, Sci. Technol. Weld. Join. 11 (2006) 170–177.
[41] J.-O. Andersson, T. Helander, L. Höglund, P. Shi, B. Sundman, Thermo-Calc & DICTRA, computational tools for materials science, Calphad 26 (2002) 273–312.
[42] J. Liu, S. Kou, Crack susceptibility of binary aluminum alloys during solidification, Acta Mater. 110 (2016) 84–94.
[43] J. Liu, S. Kou, Susceptibility of ternary aluminum alloys to cracking during solidification, Acta Mater. 125 (2017) 513–523.
[44] M. Schlesinger, M. Paunovic, Modern Electroplating, John Wiley & Sons, 2011.
[45] NPCS, Board of Consultants and Engineers, Electroplating, Anodizing & Metal Treatment Handbook, Asia Pacific Business Press Inc., 2003
[46] W. Kurz, D. Fisher, Fundamentals of Solidification, 1986, Trans Tech Publ. Switz. (1986).
[47] N. Jimenez-Mena, T. Sapanathan, J.M. Drezet, T. Pirling, P.J. Jacques, A. Simar, Residual stresses of friction melt bonded aluminum/steel joints determined by neutron diffraction, J. Mater. Process. Technol. 266 (2019) 651–661, https://doi.org/10.1016/j.jmatprotec.2018.11.030.
[48] V. Yeremenko, Y.V. Natanzon, V.I. Dybkov, The effect of dissolution on the growth of the Fe2Al5 interlayer in the solid iron-liquid aluminium system, J. Mater. Sci. 16 (1981) 1748–1756.
[49] V. Dybkov, Interaction of iron-nickel alloys with liquid aluminium, J. Mater. Sci. 28 (1993) 6371–6380.
[50] J.-M. Drezet, D. Allehaux, Application of the Rappaz-Drezet-Gremaud hot tearing criterion to welding of aluminium alloys, Hot Crack. Phenom. Welds II, Springer, 2008https://doi.org/10.1007/978-3-540-78628-3_2.
[51] Y. Tian, J.D. Robson, S. Riekehr, N. Kashaev, L. Wang, T. Lowe, A. Karanika, Process optimization of dual-laser beam welding of advanced Al-Li alloys through hot cracking susceptibility modeling, Metall. Mater. Trans. A. 47 (2016) 3533–3544.
[52] F. Yin, M. Zhao, Y. Liu, W. Han, Z. Li, Effect of Si on growth kinetics of intermetallic compounds during reaction between solid iron and molten aluminum, Trans. Nonferrous Met. Soc. China. 23 (2013) 556–561.